



Effect of pitch on nonlinear dynamics of helical vortex disturbed by long-wave instability

Yuji Hattori^{1,†} and Akihiro Hirano^{1,2}

¹Institute of Fluid Science, Tohoku University, Sendai 980-8577, Japan

²Graduate School of Information Sciences, Tohoku University, Sendai 980-8579, Japan

(Received 17 April 2024; revised 17 May 2024; accepted 27 May 2024)

The nonlinear dynamics of a helical vortex disturbed by a long-wave-instability mode is studied by direct numerical simulation. Vortex reconnection or self-reconnection of the helical vortex is shown to play a crucial role depending on the pitch of the helical vortex. For the larger pitch, a vortex ring is created after the vortex reconnection; it detaches from the remaining helical vortex, whose pitch is doubled. A vortex ring is also created for the smaller pitch; however, it forms a linked system with the remaining vortex. The topological constraint due to this linkage forces strong interaction between the different parts of the helical vortex, leading to turbulent transition.

Key words: vortex dynamics, vortex instability, turbulent transition

1. Introduction

Helical vortices occur in devices containing rotating wings, which include wind turbines, helicopters, ship propellers and other important engineering applications. In a large-scale wind farm, the wake flow of a wind turbine affects the incoming flow of the wind turbines behind it. As a result, the performance of a wind turbine in the wake of other wind turbines is often much smaller than that of a frontal wind turbine (Lee & Fields 2021).

The wake flow of a wind turbine is dominated by the helical vortices generated from the tip of the rotor blades. The helical vortices are subject to several instabilities, which can be classified into two types depending on the wavelength of the disturbance: (i) the long-wave instability, in which the wavelength of the disturbance is much larger than the vortex-core size; and (ii) the short-wave instability, in which the wavelength of the disturbance is comparable to the vortex-core size. The long-wave instability includes the pairing instability (Quaranta, Bolnot & Leweke 2015; Quaranta *et al.* 2019), the Crow instability (Crow 1970) and the mutual inductance mode (Widnall 1972). Their mechanisms can be understood in the framework of the vortex-filament approximation (Crow 1970;

† Email address for correspondence: hattori@ifs.tohoku.ac.jp

Widnall 1972; Gupta & Loewy 1974); the vorticity distribution in the vortex core does not affect the stability properties essentially, although the effective size of the vortex core affects slightly the growth rate through a cutoff in the Biot–Savart integral. In contrast, the properties of the short-wave instability, which includes the elliptic instability (Kerswell 2002; Blanco-Rodríguez & Le Dizès 2016) and the curvature instability (Hattori & Fukumoto 2003; Fukumoto & Hattori 2005; Hattori & Fukumoto 2009, 2010, 2011, 2012, 2014; Blanco-Rodríguez & Le Dizès 2017; Hattori, Blanco-Rodríguez & Le Dizès 2019), are dictated by the vorticity distribution inside the vortex core. Recent works tried to promote breakdown and turbulent transition for wake recovery by exciting long-wave instability of helical vortices (Abraham, Castillo-Castellanos & Leweke 2023; Ramos-García *et al.* 2023). In this regard, understanding the nonlinear dynamics of helical vortices after the linear regime of the long-wave instability is important not only in prediction of wake recovery but also in optimizing the method of exciting the instability to maximize the effects.

There have been many works on the dynamics of helical vortices. The long-wave instability of a single helical vortex has been captured experimentally by Quaranta *et al.* (2015); they also showed that the unstable modes are explained by the pairing instability. Alekseenko *et al.* (2016) studied the motion of a helical vortex created in a swirling flow; they showed that vortex reconnection results in either an isolated vortex ring or a vortex ring linked with the main helical vortex. However, the detailed process after the reconnection, which can lead to turbulent transition, remains unexplored. Direct numerical simulation is an ideal method to explore this process because it has several advantages over experiments; the parameters and the velocity distribution specifying the base flow and the disturbances can be prescribed at our will, while precise data of flow fields are available.

In this paper, we study the nonlinear evolution of a single helical vortex disturbed by a long-wave-instability mode by direct numerical simulation. Our objectives are to clarify the detailed processes of vortex reconnection observed by Alekseenko *et al.* (2016) and to explore the dynamics after them leading to possible turbulent transition and breakdown of the helical vortex, which are often difficult to analyse in the experiments. We will show that the evolution after the reconnection depends crucially on the pitch of the helical vortex.

2. Numerical procedure

2.1. Statement of the problem

We consider the time evolution of a helical vortex disturbed by a long-wave-instability mode in an incompressible viscous fluid. The base flow is a helical vortex with constant pitch in a cylindrical coordinate system (r, θ, z) (figure 1). The helical vortex extends infinitely in both the positive and negative z directions. The radius of the cylinder of which surface includes the centreline helix is R , while the spatial period in the z direction is $2\pi L$; we call L/R the reduced pitch as in Delbende, Rossi & Daube (2012). The vorticity is concentrated in the vicinity of the centreline helix.

2.2. Numerical methods

The numerical procedure consists of three steps: (i) a base flow is obtained as a quasisteady state by solving the Navier–Stokes equations; (ii) a long-wave-instability mode is obtained by integrating the linearized Navier–Stokes equations for a sufficiently long time; and (iii) the time evolution of a helical vortex disturbed by the long-wave-instability mode is obtained by solving the Navier–Stokes equations. The numerical method for solving the Navier–Stokes equations is similar to that used in Hattori *et al.* (2019). Namely, for the

Helical vortex disturbed by long-wave instability

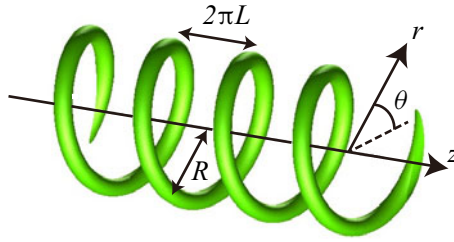


Figure 1. Schematic diagram of helical vortex in the cylindrical coordinate system. The helical vortex extends infinitely in the $+z$ and $-z$ directions with constant reduced pitch L/R .

spatial discretization, the sixth-order accurate compact scheme (Lele 1992) was used in the r direction, while the Fourier spectral method was used in the θ and z directions. The Poisson equation was decomposed into a set of ordinary differential equations for a single Fourier mode, which were also solved by the sixth-order accurate compact scheme. For the temporal discretization, the Crank–Nicolson scheme was used for the viscous terms, while the second-order Adams–Bashforth method was used for the other terms.

In the first step, the initial vorticity field is given by a Gaussian distribution:

$$\boldsymbol{\omega} = \omega_0 e^{-\rho^2/a_0^2} \mathbf{e}_B, \quad \mathbf{e}_B = \left(1 + \frac{r^2}{L^2}\right)^{-1/2} \left(\mathbf{e}_z + \frac{r}{L} \mathbf{e}_\theta\right), \quad (2.1a,b)$$

where ρ is the distance from the centreline helix, ω_0 is the maximum vorticity, a_0 is the core radius, and \mathbf{e}_z and \mathbf{e}_θ are the unit vectors in the z and θ directions, respectively. It is pointed out that \mathbf{e}_B is tangential to the centreline helix when $r = R$. The above initial condition is not a steady solution even in a suitable rotating and/or translating frame taking account of the motion of the helical vortex due to the self-induced velocity. However, it reaches a quasisteady state after a certain long time through a relaxation process due to viscous diffusion (Selçuk, Delbende & Rossi 2017). The initial radius of the vortex core grows with time approximately as $a^2 = a_0^2 + 4\nu t$, where ν is the kinematic viscosity and t is the time; thus, a_0 was chosen so that the value of a after relaxation becomes a prescribed value.

In the second step, we move to an inertial frame translating with the helical vortex in which it is quasisteady. The so-called ‘frozen-in’ assumption is employed: the time evolution of the base flow obtained in the first step is neglected because its time scale is much larger than the instability. Thanks to the helical symmetry of the base flow, the linear disturbances can be decomposed into modes of the following form which evolve independently:

$$\mathbf{u}'(r, \theta, z, t) = \hat{\mathbf{u}}(r, \varphi, t) e^{ik_z z} + \text{c.c.}, \quad (2.2)$$

where $\varphi = \theta - (z/L)$ and k_z is the wavenumber in the z direction. For the initial disturbances, we chose a single mode with a velocity distribution $\hat{\mathbf{u}}$ randomized and concentrated near the vortex core. Then, by integrating the Navier–Stokes equations linearized about the frozen-in base flow for a sufficiently long time, the most unstable eigenmode is obtained as it becomes much larger than the other modes.

In the third step, the initial condition was obtained by adding the unstable mode obtained in the second step with a small amplitude to the base flow. It is pointed out that in the first and third steps the equations are solved in the static frame of reference in which the flow is at rest at infinity, while the equations in the moving frame as explained above are solved in the second step.

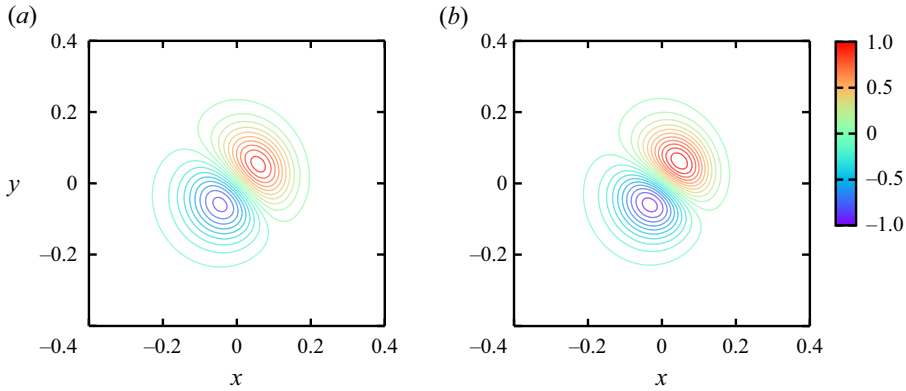


Figure 2. Structure of long-wave-instability mode shown by contours of $\omega' \cdot e_B$. $k_z L = 1/2$. Here (a) $L/R = 0.3$, (b) $L/R = 0.2$.

The simulation parameters were chosen as follows. The Reynolds number based on the circulation Γ of the helical vortex was $Re_\Gamma = \Gamma/\nu = 15\,700$ in the first and second steps; it is reduced to $Re_\Gamma = 3925$ in the third step because small-scale structures which emerge after turbulent transition could not be resolved sufficiently at $Re_\Gamma = 15\,700$. The core size of the helical vortex normalized by the curvature radius $(R^2 + L^2)/R$ was set to $aR/(R^2 + L^2) = 0.1$. Two values of the reduced pitch were considered: $L/R = 0.2$ and 0.3 . The wavenumber of the disturbance is set to $k_z L = 1/2$, at which the growth rate of the long-wave instability is maximum (Widnall 1972; Quaranta *et al.* 2015). For the domain of calculation, the outer boundary was placed far away from the helical vortex at $r = 100R$ to minimize the effect of the slip boundary conditions using stretching grids in the r direction; the axial size of the domain was $4\pi L$ to accommodate the wavenumber $k_z L = 1/2$. The minimum grid size in r was $\Delta r_{min} = 4.75 \times 10^{-3}R$, while the grid size in z was $4.91 \times 10^{-3}R$. The number of grid points was $N_r \times N_\theta \times N_z = 695 \times 960 \times 256$ for $L/R = 0.2$, while N_z was replaced with 384 for $L/R = 0.3$. The values in the rest of the paper are scaled by the circulation Γ and the radius of the cylinder R unless stated explicitly. Throughout the simulation the impulse, which is an invariant in viscous flows, was conserved within $6.4 \times 10^{-5} \%$ and $2.3 \times 10^{-2} \%$ errors for $L/R = 0.2$ and 0.3 , respectively, confirming the sufficient accuracy of the numerical simulation.

2.3. Linear instability

Here we briefly summarize the results on the long-wave instability. The growth rates turned out to be $\sigma = 0.236$ and 0.504 for $L/R = 0.3$ and 0.2 , respectively. When normalized by $h = 2\pi L$ instead of R as the length scale as in Quaranta *et al.* (2015), they are $2h^2\sigma/\Gamma = 1.68$ and 1.59 for $L/R = 0.3$ and 0.2 , respectively; they are close to the theoretical value $\pi/2$ and the improved theoretical values given by (2.13) of Quaranta *et al.* (2015):

$$\sigma_p^*(k) = 2\pi k \left[1 - k \left(1 + \left(\frac{L}{R} \right)^2 \right)^{-1} \right], \quad (2.3)$$

which gives 1.70 and 1.63, respectively, at $k = 1/2$. In figure 2, the mode structures for $L/R = 0.3$ and 0.2 are shown by contours of $\omega' \cdot e_B$, where ω' is the vorticity of the disturbance, on a plane perpendicular to e_B at $r = R$, while the origin coincides with the centreline helix. In this figure, the unit vectors are chosen as $e_x = e_r$ and $e_y = e_B \times e_r$. The

modes are displacement modes which deform the helix in the direction of the line $y = x$ (Quaranta *et al.* 2015; Selçuk, Delbende & Rossi 2018).

3. Results

3.1. Results for $L/R = 0.3$

First, we show the results for the larger reduced pitch $L/R = 0.3$. Figure 3 shows the time evolution of the helical vortex visualized by the isosurface of the magnitude of vorticity; it is coloured by the axial component of vorticity ω_z with red and blue corresponding to positive and negative values, respectively. The value for the isosurface is $|\omega| = 0.3\sqrt{\Omega/R^3}$, where $\Omega = \int |\omega|^2 dV$ is the enstrophy and $dV = r dr d\theta dz$. In this figure, we set the axial size of the domain for visualization to $8\pi L$ to include two adjacent numerical domains; this is to show clearly the structures near the periodic boundaries $z = 0$ or $4\pi L$. Thus, four pitches of the helical vortex exist initially in the domain for visualization since the periodic unit of the numerical domain involves two pitches.

At $t = 17.5$ (figure 3a), the instability is still in a linear regime as the distance between the adjacent spirals as well as the distance from the z axis become non-uniform as in Quaranta *et al.* (2015). Nonlinear deformation is observed at $t = 23$ (figure 3b) as the spirals of smaller radius get close to those of larger radius from inside of the helical vortex, forming vortex-ring-like structures. They move outward owing to the self-induced velocity (figure 3c). Vortex reconnection is in progress from $t \approx 30$ to $t \approx 35$, the so-called ‘bridges’ being observed at $t = 31, 33$ and 35 (figure 3d–f). Vortex rings detach from the helical vortex and propagate away from it (figure 3g). The pitch of the remaining helical vortex is doubled as the number of spirals is reduced from four at $t = 17.5$ (figure 3a) to two at $t = 65$ (figure 3h). The time evolution is also shown by the supplementary movie available at <https://doi.org/10.1017/jfm.2024.529>.

Figures 4(a) and 4(c) show the time evolution of the energy $E = \int |\mathbf{u}|^2 dV$, the enstrophy Ω and the helicity $H = \int \mathbf{u} \cdot \boldsymbol{\omega} dV$. It is pointed out that the non-zero value of the initial helicity is due to the self-induced velocity of the helical vortex, which has an e_B component. The three quantities decrease initially due to viscous diffusion. At $t \approx 22$, however, the enstrophy turns from decreasing to increasing as the adjacent spirals get close and are stretched. The increase accelerates during the vortex reconnection in which thin vortex tubes are generated. The helicity also increases as a result of vortex reconnection. The rate of decay of the energy, which is proportional to the enstrophy as $dE/dt = -2\nu\Omega$, increases only slightly during the vortex reconnection as the local maximum of the enstrophy at $t \approx 35$ is smaller than the initial value; transition to turbulence does not occur.

3.2. Results for $L/R = 0.2$

Next, we show the results for the smaller reduced pitch $L/R = 0.2$. Figure 5 shows the time evolution of the helical vortex visualized in the same way as for $L/R = 0.3$, while the direction of the helical vortex is chosen to show the whole process clearly. The linear deformation at $t = 8$ (figure 5a) is similar to the case $L/R = 0.3$ at $t = 17.5$ (figure 3a). At $t = 12.5$ (figure 5b), the smaller spirals go through the larger spirals, which resembles the leap-frogging of coaxial vortex rings (Oshima 1978). At $t = 14.75$ (figure 5c), there arise two possibilities of vortex reconnection marked by the circles. It turns out that the first reconnection occurs in the upper-left region shown by the red circle as bridges form at $t = 15.5$ (figure 5d). Vortex rings appear as a result of reconnection; they wrap around the deformed remaining vortex, forming a linked system of vortices (figure 5e), which will be shown in detail later in figure 7. This linkage imposes a topological constraint on

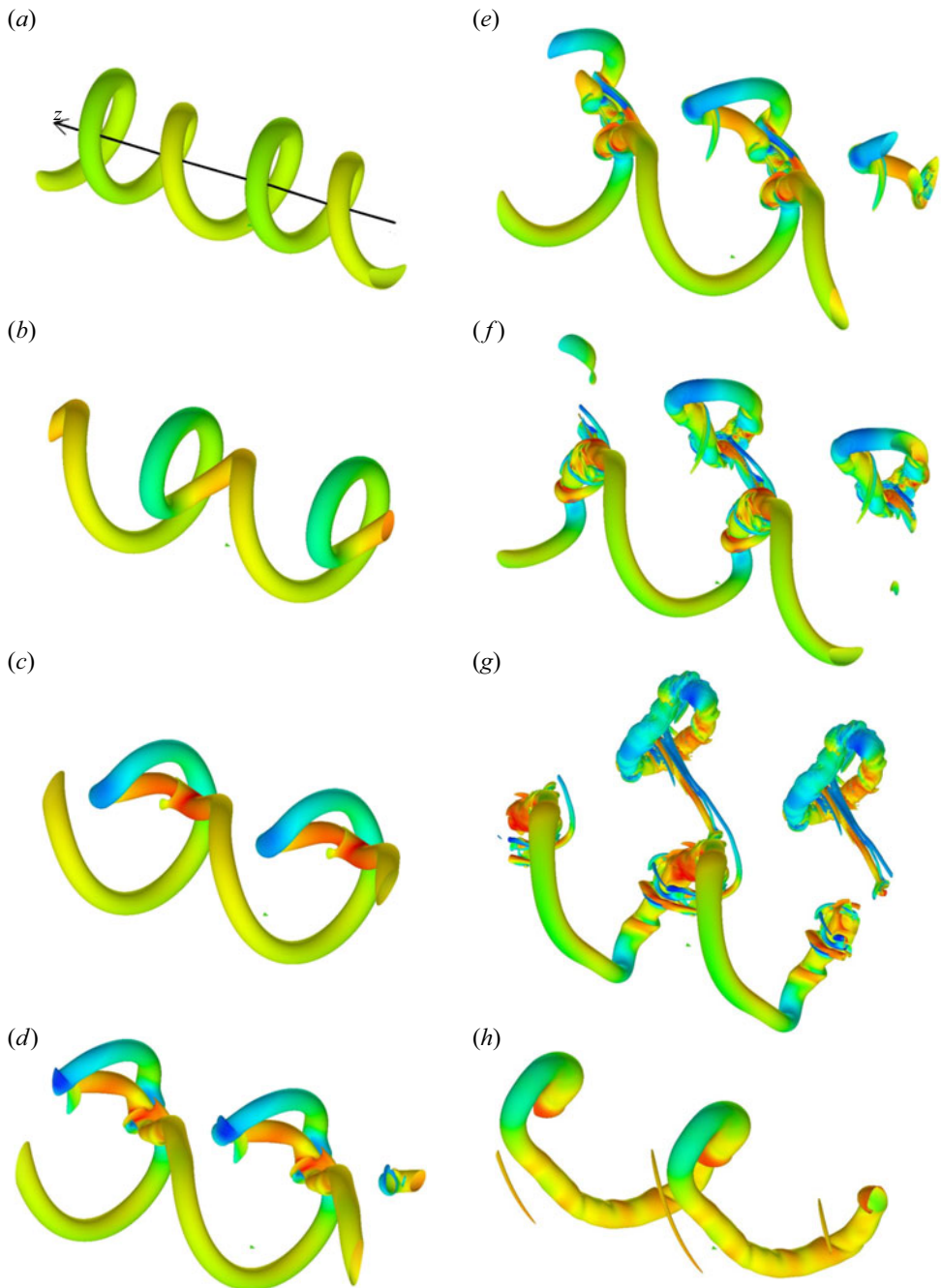


Figure 3. Time evolution of helical vortex with $L/R = 0.3$. The isosurface of the magnitude of vorticity coloured by the axial component of vorticity ω_z . Here $t =$ (a) 17.5, (b) 23, (c) 28, (d) 31, (e) 33, (f) 35, (g) 40, (h) 65.

the vortex motion forcing strong interaction between vortex tubes. As a result, many thin vortex tubes emerge around the vortex rings and the deformed vortex (figure 5f); finally the flow becomes turbulent as it is dominated by small-scale structures (figure 5g,h). The time evolution is also shown by the supplementary movie.

Helical vortex disturbed by long-wave instability

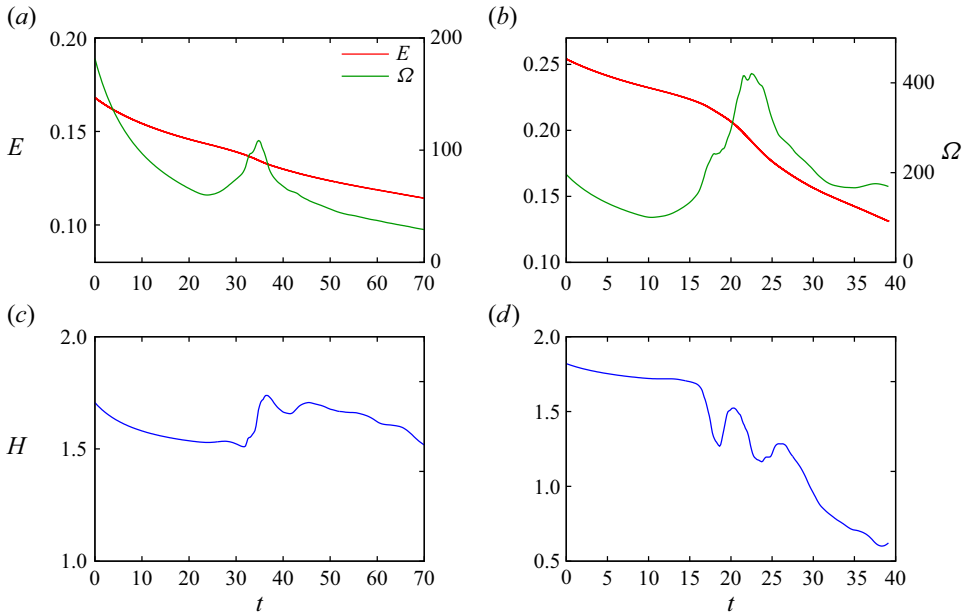


Figure 4. Time evolution of (a,b) energy, enstrophy and (c,d) helicity. Here (a,c) $L/R = 0.3$, (b,d) $L/R = 0.2$.

The time evolution of the energy, the enstrophy and the helicity is shown in figure 4. The enstrophy reaches $\Omega \approx 420$, which is twice as large as the initial value, at $t = 18.5$ when small-scale structures develop. Rapid changes of helicity are observed in figure 4(d). The first change in $16 \lesssim t \lesssim 18$ corresponds to the first reconnection. The second change in $18.8 \lesssim t \lesssim 19.5$ and the third change in $21 \lesssim t \lesssim 22.8$ are also signs of reconnection; in fact, successive reconnections occur, although they become less clear as the flow becomes turbulent.

Figure 6 shows the compensated one-dimensional energy spectrum at two instants after the first reconnection. The velocity field is Fourier transformed in the z direction and the resulting spectrum is summed up at the regions on the (r, θ) plane where the rate of dissipation averaged in z is larger than 30% of its maximum. It is pointed out that the wavenumber is normalized by the Kolmogorov length η , while the rate of energy dissipation ε is used to normalize the compensated energy spectrum. The spectrum shows the Kolmogorov scaling, although the range is narrow at $t = 18.25$; it confirms that the flow becomes turbulent after strong interaction of vortices.

The structure of the vortices are elucidated in figure 7. Here we apply a Gaussian filter to the vorticity as

$$\bar{\omega}_i(\mathbf{x}) = \int G(\mathbf{x} - \mathbf{x}') \omega_i(\mathbf{x}') d\mathbf{x}', \quad G(\mathbf{x}) = \left(\frac{6}{\pi \bar{\Delta}^2} \right)^{1/2} \exp(-6|\mathbf{x}|^2 / \bar{\Delta}^2), \quad (3.1a,b)$$

with filter size $\bar{\Delta} = 64\Delta r_{min}$ to remove small-scale structures. The isosurface of the magnitude of the filtered vorticity is shown in figure 7 for $|\bar{\omega}| = 0.3\sqrt{\Omega/R^3}$. It is pointed out that the point and line of sight are different from those in figure 5; they are chosen to clarify the topological change of the vortices. Figure 7 confirms the following: before

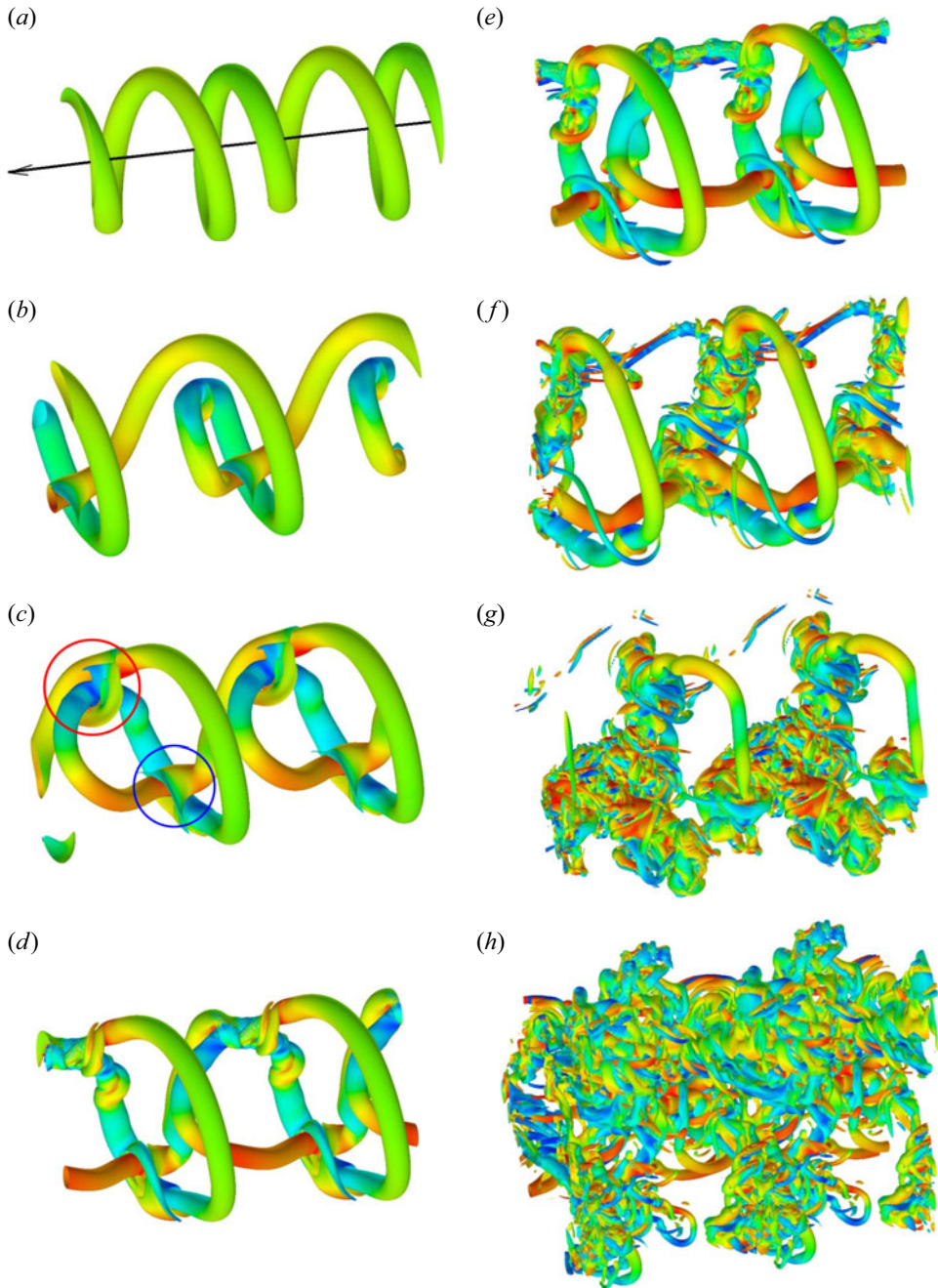


Figure 5. Time evolution of helical vortex with $L/R = 0.2$. The isosurface of the magnitude of vorticity coloured by the axial component of vorticity ω_z . Here $t =$ (a) 8, (b) 12.5, (c) 14.75, (d) 15.5, (e) 16.13, (f) 17.38, (g) 19.25, (h) 23.38.

the first reconnection the helical vortex is deformed but is still connected (figure 7a); the bridges are observed during the reconnection (figure 7b); and vortex rings wrap around the deformed vortex after the reconnection (figure 7c).

Helical vortex disturbed by long-wave instability

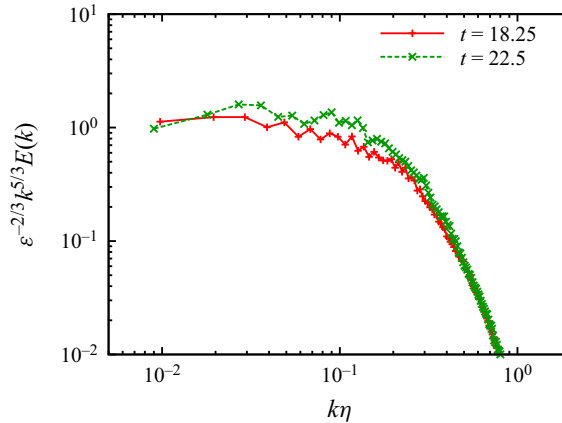


Figure 6. Compensated one-dimensional energy spectrum. Here $L/R = 0.2$, $t = 18.25, 22.5$.

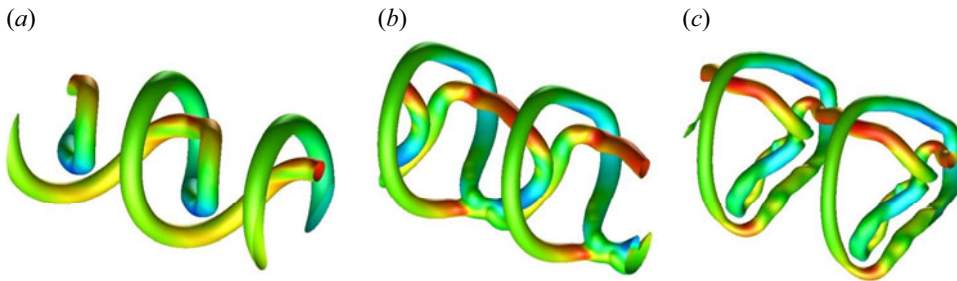


Figure 7. Reconnection process shown by isosurface of magnitude of filtered vorticity. The isosurface is coloured by the axial component of filtered vorticity \bar{w}_z . Here $L/R = 0.2$, $t = (a) 13, (b) 15.38, (c) 16.63$.

4. Concluding remarks

The time evolution of the helical vortex disturbed by a long-wave-instability mode has been studied by direct numerical simulation for the two values of the reduced pitch $L/R = 0.2$ and 0.3 . Self-reconnection of the helical vortex plays an important role in both cases. For $L/R = 0.3$, a vortex ring detaches from the helical vortex after the reconnection; the pitch of the helical vortex is doubled. For $L/R = 0.2$, on the other hand, the vortex ring created after the first reconnection and the remaining helical vortex form a linked system of vortices. The process of reconnection is similar to that observed in Alekseenko *et al.* (2016). However, the present numerical results have clarified the detailed process under perfectly prescribed conditions. More importantly, the long-time evolution after the reconnection has revealed the difference between the two cases: for $L/R = 0.2$, the turbulent transition occurs as a consequence of topological constraint, while it does not occur for $L/R = 0.3$.

Implication to practical applications is discussed below. In the present work, the Reynolds number is much smaller than that of the helical vortices which occur in wind turbines, while the core size and the pitch are larger. There will be some differences in the process between the two cases. The essential dynamics at least up to the linear regime would be similar because the properties of the long-wave instability do not depend very much on the core size and the Reynolds number; in fact, the process resembling leap-frogging has been observed not only in the present work but also in the experiments

(Quaranta *et al.* 2015). However, the fully nonlinear evolution after the leap-frogging can be different. Vortex tubes should get close within the order of the core size to reconnect. When the core size is small, the vortex tubes will interact and deform in more complex ways than the present results, which may lead to different topology of vortices. Although the topological constraint due to linkage of the vortex tubes is expected to be important also in the helical vortices in wind turbines, the detailed process should be investigated; this is one of the future works, which also include the role of short-wave instabilities (Hattori & Fukumoto 2009, 2010, 2011, 2012, 2014; Blanco-Rodríguez & Le Dizès 2016, 2017; Hattori *et al.* 2019) and the effects of torsion (Ricca 1994).

Supplementary movies. Supplementary movies are available at <https://doi.org/10.1017/jfm.2024.529>.

Funding. This work was supported by JSPS KAKENHI 21H01242. Numerical calculations were performed on AFI-NITY at the Institute of Fluid Science, Tohoku University.

Declaration of interests. The authors report no conflict of interest.

Author ORCIDs.

Yuji Hattori <https://orcid.org/0000-0002-1601-6416>.

REFERENCES

- ABRAHAM, A., CASTILLO-CASTELLANOS, A. & LEWEKE, T. 2023 Simplified model for helical vortex dynamics in the wake of an asymmetric rotor. *Flow* **3**, E5.
- ALEKSEENKO, S.V., KUIBIN, P.A., SHTORK, S.I., SKRIPKIN, S.G. & TSOY, M.A. 2016 Vortex reconnection in a swirling flow. *JETP Lett.* **103**, 455–459.
- BLANCO-RODRÍGUEZ, F.J. & LE DIZÈS, S. 2016 Elliptic instability of a curved Batchelor vortex. *J. Fluid Mech.* **804**, 224–247.
- BLANCO-RODRÍGUEZ, F.J. & LE DIZÈS, S. 2017 Curvature instability of a curved Batchelor vortex. *J. Fluid Mech.* **814**, 397–415.
- CROW, S.C. 1970 Stability theory of a pair of trailing vortices. *AAIA J.* **8**, 2172–2179.
- DELBENDE, I., ROSSI, M. & DAUBE, O. 2012 DNS of flows with helical symmetry. *Theor. Comput. Fluid Dyn.* **26**, 141–160.
- FUKUMOTO, Y. & HATTORI, Y. 2005 Curvature instability of a vortex ring. *J. Fluid Mech.* **526**, 77–115.
- GUPTA, B.P. & LOEWY, R.G. 1974 Theoretical analysis of the aerodynamics stability of multiple, interdigitated helical vortices. *AIAA J.* **12**, 1381–1387.
- HATTORI, Y. & FUKUMOTO, Y. 2003 Short-wavelength stability analysis of thin vortex rings. *Phys. Fluids* **15**, 3151–3163.
- HATTORI, Y. & FUKUMOTO, Y. 2009 Short-wavelength stability analysis of a helical vortex tube. *Phys. Fluids* **21**, 014104.
- HATTORI, Y. & FUKUMOTO, Y. 2010 Short-wave stability of a helical vortex tube: the effect of torsion on the curvature instability. *Theor. Comput. Fluid Dyn.* **24**, 363–368.
- HATTORI, Y. & FUKUMOTO, Y. 2011 Erratum: short-wavelength stability analysis of a helical vortex tube. *Phys. Fluids* **23**, 049901.
- HATTORI, Y. & FUKUMOTO, Y. 2012 Effects of axial flow on the stability of a helical vortex tube. *Phys. Fluids* **24**, 054102.
- HATTORI, Y. & FUKUMOTO, Y. 2014 Modal stability analysis of a helical vortex tube with axial flow. *J. Fluid Mech.* **738**, 222–249.
- HATTORI, Y., BLANCO-RODRÍGUEZ, F.J. & LE DIZÈS, S. 2019 Numerical stability analysis of a vortex ring with swirl. *J. Fluid Mech.* **878**, 5–36.
- KERSWELL, R. 2002 Elliptical instability. *Annu. Rev. Fluid Mech.* **34**, 83–113.
- LEE, J.C.Y. & FIELDS, M.J. 2021 An overview of wind-energy-production prediction bias, losses, and uncertainties. *Wind Energy Sci.* **6**, 311–365.
- LELE, S.K. 1992 Compact finite-difference schemes with spectral-like resolution. *J. Comput. Phys.* **103**, 16–42.
- OSHIMA, Y. 1978 The game of passing-through of a pair of vortex rings. *J. Phys. Soc. Japan* **45**, 660–664.
- RAMOS-GARCÍA, N., ABRAHAM, A., LEWEKE, T. & SØRENSEN, J.N. 2023 Multi-fidelity vortex simulations of rotor flows: validation against detailed wake measurements. *Comput. Fluids* **255**, 105790.

Helical vortex disturbed by long-wave instability

- RICCA, R.L. 1994 The effect of torsion on the motion of a helical vortex filament. *J. Fluid Mech.* **273**, 241–259.
- QUARANTA, H.U., BOLNOT, H. & LEWEKE, T. 2015 Long-wave instability of a helical vortex. *J. Fluid Mech.* **780**, 687–716.
- QUARANTA, H.U., BRYNJELL-RAHKOLA, M., LEWEKE, T. & HENNINGSON, D.S. 2019 Local and global pairing instabilities of two interlaced helical vortices. *J. Fluid Mech.* **863**, 927–955.
- SELÇUK, C., DELBENDE, I. & ROSSI, M. 2017 Helical vortices: quasiequilibrium states and their time evolution. *Phys. Rev. Fluids* **2**, 084701.
- SELÇUK, C., DELBENDE, I. & ROSSI, M. 2018 Helical vortices: linear stability analysis and nonlinear dynamics. *Fluid Dyn. Res.* **50**, 011411.
- WIDNALL, S.E. 1972 The stability of a helical vortex filament. *J. Fluid Mech.* **54**, 641–663.